SPECIAL ISSUE - RESEARCH ARTICLE

WILEY ENERGY RESEARCH
INTERNATIONAL JOURNAL OF

Interfacial transport characteristics between heterogeneous porous composite media for effective mass transfer in fuel cells

Jiawen Liu | Seungho Shin | Sukkee Um [iD]

Department of Mechanical Engineering, Hanyang University, Seoul, South Korea

Correspondence
Sukkee Um, Department of Mechanical Engineering, Hanyang University, 222 Wangsimni-ro, Seongdong-gu, Seoul 04763, South Korea.
Email: sukkeeum@hanyang.ac.kr

Summary

In this study, a comprehensive computational model based on a full statistical approach was developed to investigate the heterogeneous mass transport properties in the metal foam channels, gas diffusion layers (GDLs), and microporous layers (MPLs) of polymer electrolyte fuel cells (PEFCs) at the 95% confidence level. A series of channels, GDLs, and MPLs were, respectively, generated to reflect the random heterogeneous structures and transport characteristics. The critical hydrophobic pore radius in the mixed wettability GDLs was computed by applying a modified Leverett function. Furthermore, the gas transport phenomenon through a sufficient number of porous transport media was simulated using a D3Q19 (ie, three-dimensional, 19 velocities) lattice Boltzmann method, and the corresponding mass transport characteristics were mathematically presented as a function of the porosity. The permeabilities in the channels, GDLs, and MPLs were derived from the pressure gradient and the simulated velocity distribution. It was found that the effective mass diffusion coefficient in the GDLs is mainly influenced by molecular diffusion. Nevertheless, Knudsen diffusion is the dominant mass transfer mechanism in the MPLs, because of small pore diameters. In addition, critical hydrophobic pore radius was derived using a modified Leverett function, which enables to estimate the fraction of pores larger than the critical pore radius in GDLs for effective water transport. Moreover, the interfacial areal contact ratio between two adjacent porous media (ie, channel/GDL and GDL/MPL) was calculated. The calculations indicated that the variation in the local porosity of the porous media has a significant influence on the interfacial connections. The proposed model is expected to improve the prediction performance of porous heterogeneous transport media in electrochemical energy systems and the optimization of porous media structures.

KEYWORDS
fuel cells, heterogeneous transport porous media, interfacial contact ratio, interfacial pore distribution, lattice Boltzmann method, mass transfer, statistical analysis

1 | INTRODUCTION

Fuel cells have attracted significant attention over the past few years as a new energy technology that converts chemical energy into electrical energy. In polymer electrolyte fuel cell (PEFC) systems, as shown in Figure 1A, the reactant gases flow through the channels, gas diffusion layers (GDLs), and microporous layers (MPLs) to the porous catalyst layers. Metal foam channels are highly porous lightweight structures with flexible permeabilities and high specific surface areas,[1] thus providing excellent heat and mass transfer characteristics for fuel cells. GDLs are located between the neighboring flow channels and catalyst layers, and they were designed to provide diverse void spaces for mass transfer including reactant supply and product removal to and from the catalytic sites, in addition to mechanical strength as an electrode support[2] by absorbing the external clamping pressure. Furthermore, electrons and heat in fuel cells are mainly transferred through carbon fibers of GDLs. As seen in Figure 1B, GDLs are random porous media with intrinsically heterogeneous morphological structures composed of nonwoven carbon fibers, which show highly anisotropic microstructures and allow principal conductive paths for electrons and heat transfer. Polytetrafluoroethylene (PTFE), which is a highly hydrophobic material, was adopted on the surface of GDLs to prevent water flooding and pore blockage. Microporous layers (MPLs) are thin (thicknesses of approximately 5-20 μm) layers composed of carbon particles, polymeric binder, and PTFE,[2] which are applied between GDLs and catalyst layers to aid in water management and

enhance the electrical contact. Based on the overall roles of various fuel cell components, the performance of the mass transport through the channels, GDLs, and MPLs has significant effects on the neighboring catalyst layers where electrochemical reactions occur. Hence, it is essential to simulate the mass transport phenomena within the composite porous structures, to evaluate the interfacial properties, and to explicate the structural influences on the performances of heterogeneous porous media for fuel cell applications.

Recently, extensive studies have applied numerous experimental and numerical techniques to investigate the mass transport characteristics of heterogeneous porous media in fuel cells. Kumar and Reddy[3] developed a three-dimensional numerical mass transfer model for PEMFC with metal foam in the flow fields. They evaluated the performance of fuel cells with various permeability levels of metal foam flow fields. They found that a more uniform distribution of current density was obtained with metal foams than with traditional channel-type flow fields. Therefore, they proposed that metal foam flow fields with proper permeability would have a positive effect on the fuel cell performance. Tsai et al[4] compared the various conventional flow-field designs of fuel cells. Their experimental results showed that the metal foam flow fields have higher air utilization rate and show better power density than the traditional serpentine flow fields. They revealed that the metal foam flow fields improved the fuel cell performance. Paek et al[5] reported their experimental results on high porosity metal foams with measured permeability. Feser et al[6] developed robust radial permeability experiments to characterize in-plane permeability of GDLs. Gostick et al[7] measured the gas permeabilities of several commercial GDLs in three perpendicular directions, which indicated the anisotropic permeabilities of GDLs. Similarly, Kramer et al[8,9] measured the through- and in-plane diffusion coefficients of commercial GDLs and revealed that the tortuosity of GDLs is highly dependent on their structures. The diffusion coefficient in carbon paper GDLs was also measured using various experimental techniques such as a Loschmidt cell[10] and an ex situ electrochemical limiting-current method.[11,12] The in- and through-plane gas permeabilities were measured for different GDL materials by Ihonen et al.[13] They found that the ratios of in- and through-plane permeability are different in different GDL materials. In addition, they revealed that the GDLs which apply MPLs had lower permeabilities than the bare GDLs because of the small permeability of the MPLs. Instead of direct measurements, the properties of MPLs are typically measured by comparing the changes in the characteristics of the bare carbon paper formed by the application of MPLs.[10,14,15] The through-plane permeability of
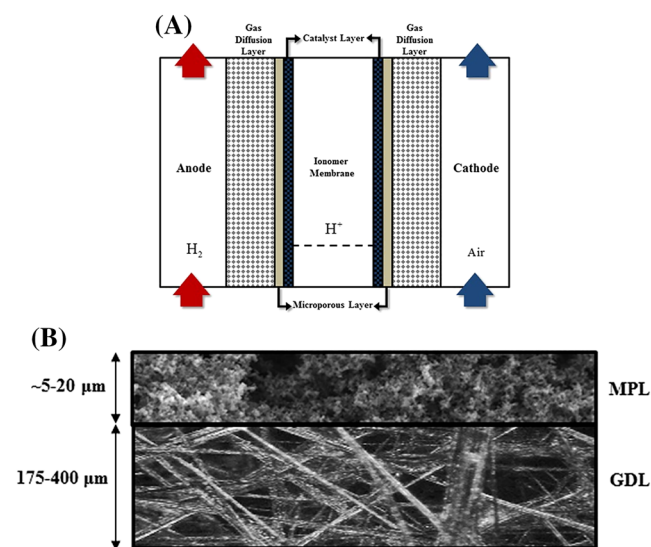
FIGURE 1 A, Mass transfer schematic of PEFCs. B, SEM images of porous transport media structures in fuel cells [Colour figure can be viewed at wileyonlinelibrary.com]

commercial bare GDLs and GDLs coated with MPLs was, respectively, measured by Williams et al.[14] They concluded that MPLs significantly decreased the overall through-plane permeability caused by their small pores. The abovementioned experimental studies were effective in revealing the mass transport properties of porous media. However, experimental studies are limited with respect to the direct measurement of MPL properties and the evaluation of the representative fluidic transport characteristics of various random porous structures.

In some numerical studies, lattice Boltzmann methods (LBMs) were applied to model the fluid flow in reconstructed porous structures of fuel cells.[16-22] Beugre et al[16] simulated single-phase incompressible flow in metallic foam using an LBM. Park et al[17] investigated the single-phase gas flow in a carbon cloth GDL by employing a three-dimensional 15-speed lattice Boltzmann (LB) model. Moreover, the permeability was calculated, and it was found to be highly dependent on the fiber orientation. Transport properties with pore interconnections were considered by Wu and Jiang.[18] The structural and mass transfer properties were determined, which include the pore size distribution, gas diffusivity, and tortuosity in a GDL using an LBM. Ostadi et al[19] applied a validated LBM to evaluate the properties of a GDL-MPL assembly and then estimated the tortuosity and permeability of the MPL.

In addition, interfacial properties between the components of the fuel cells were investigated in several studies.[23-27] You and Liu[23] modeled the flow and transport in the combined gas channel and porous gas diffusion media in the fuel cell. Lai et al[24] applied a finite element method to predict the contact resistance between the bipolar plates and GDLs. However, these studies simplified the pore structures and physical characteristics of the interfacial region, and the heterogeneous structures of the transport media could not be accurately reflected. Moreover, it should be noted that heterogeneous transport porous media exhibit intrinsically complex random structures. Hence, a sufficient number of samples is required to summarize the general characteristics of these media.

This study aims three major objectives: (1) stochastic modeling of nanoscale/microscale random structures of porous transport media, (2) statistical prediction and modification of mass transport characteristics throughout the porous layers using probability theories, and (3) statistical analysis of the contact properties at the interfaces between adjacent porous layers. In contrast to the previous studies, random structures of heterogeneous porous transport media, which include metal foam channels, GDLs, and MPLs, were stochastically modeled. A comprehensive full statistical approach was conducted to investigate the pore interconnections and effective transport characteristics in these porous media at a 95% confidence level. The hydrophobic pore distribution, which is related to water condensation in the mixed wettability GDLs, was estimated using a modified Leverett function. Subsequently, a single-phase three-dimensional LBM was proposed to simulate the microscale mass transport phenomena within a series of porous media with various porosities. The outlet fluid flow characteristics of the porous media were applied to the neighboring porous composites to maintain the continuity of the flow properties. Furthermore, the effective mass transport properties (ie, the permeability, tortuosity, and effective mass diffusion coefficient) were then predicted by numerically tracking the local velocity and pressure of the reactant flow. Finally, the interfacial areal contact ratio between adjacent layers was estimated to clarify the effects of the local porosities of the porous media.

2 | METHODOLOGIES

2.1 | Numerical model assumptions

The following assumptions were included in the statistical model applied in this study:

- Three-dimensional porous media domain before compression.
- Ternary components (carbon fibers, 5 wt% PTFE loading,[2,28] and pores) of GDLs and ternary components (77 wt% carbon particles, 23 wt% PTFE loading,[28] and pores) of MPLs with inhomogeneous random probability distributions.
- The carbon fibers by straight cylinders with a uniform diameter of 6 μm,[29] which extended from boundary to boundary without overlapping.
- A single-phase 353 K oxidant incompressible inlet gas flow at 1 atm simulating a PEFC cathode.
- The produced water in the vapor form.
- Constant temperature throughout the domain.
- Constant pressure at the boundaries of the domain.
- A 95% confidence level.[30]

2.2 | Porous transport media structure modeling

In this study, a stochastic computational model, which was based on the statistical information of porous media, was adapted to construct sets of metal foam channel, GDL, and MPL structures. A 95% confidence level was applied for the statistical analysis with trial numbers of

20, 15, and 30 for the channels, GDLs, and MPLs, respectively. Porosity is an essential parameter of porous media which controls the volume ratio of solids and pores, and it is given by

$$\varepsilon = \frac{V^{po}}{V} = 1 - \frac{V^s}{V} \qquad (1)$$

where V^{po}, V, and V^s denote the pore volume, total volume of the computational domain, and solid volume, respectively. In this study, the initially predetermined bulk volume fraction of the porous media is defined as superficial porosities. A random number generation process was applied to assume the pore and solid lattice units' distributions and to satisfy the given superficial pore volume fraction (ie, porosity).[31] It should be noted that the porosities of the reconstructed porous media in this study may differ from the initially predetermined average values. However, the final averaged porosities were approximately equal to the prescribed values. Therefore, it is advisable to carefully identify each component of porous media by occupying them with different clusters.

2.2.1 | Metal foam channel microstructure modeling

Metal foams consist of solid metals with gas-filled pores, made by injecting gas bubbles into liquid metals to form pore spaces that occupy a large portion of the volume[32] in the molten metals. Accordingly, in this study, metal foam channels were generated by randomly creating spheres with uniform radii in the three-dimensional solid domain. This generation procedure was implemented until the desired porosity was achieved. Figure 2A presents a three-dimensional constructed highly porous metal foam channel with a porosity of 0.9 and side length of 0.45 mm.

2.2.2 | Carbon paper GDL

For the GDL microstructure model, the two end points of each fiber were randomly selected on the boundaries in the GDL domain with a thickness of 200 μm. Furthermore, straight-cylindrical carbon fibers with uniform diameters of 6 μm that extended from boundary to boundary were randomly placed layer by layer in the domain. Moreover, the bulk densities of the carbon fiber and PTFE ($\rho_{carbon} = 1.9$ g cm^{-3} and $\rho_{PTFE} = 2.16$ g cm^{-3})[33] were used to convert the mass-based parameters of the GDLs into the equivalent volume-based compositions, to match the predetermined average porosities

(A)

(B)

(C)
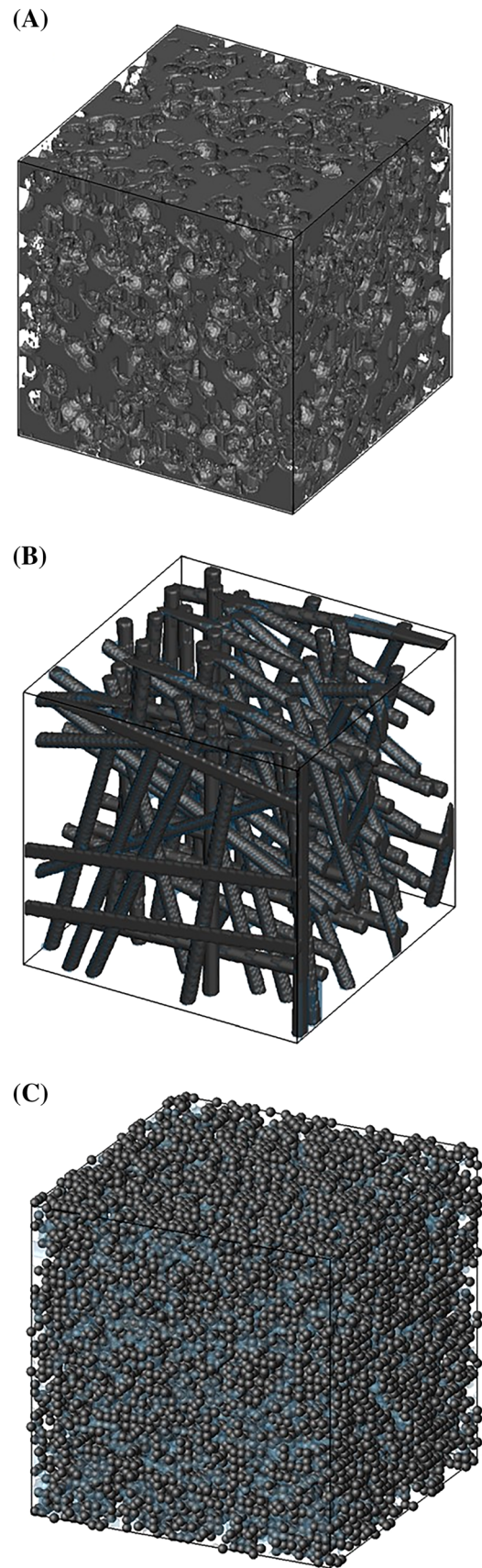
FIGURE 2 Three-dimensional structures of A, MPL, B, GDL, and C, fine mesh flow fields [Colour figure can be viewed at wileyonlinelibrary.com]

according to the following equations:

$$\phi^{\text{carbon}} = m_{\text{carbon}} \frac{1}{\rho_{\text{carbon}}} = m_{\text{PTFE}} \left(\frac{1 - \omega_{\text{PTFE}}}{\omega_{\text{PTFE}}} \right) \frac{1}{\rho_{\text{carbon}}} \quad (2)$$

$$\phi^{\text{PTFE}} = m_{\text{PTFE}} \frac{1}{\rho_{\text{PTFE}}} \quad (3)$$

$$\phi^{\text{PTFE}} + \phi^{\text{carbon}} + \varepsilon = 1 \quad (4)$$

where ϕ^{PTFE} and ϕ^{carbon} are the volume fractions of the PTFE and carbon, respectively. m_{PTFE} and m_{carbon} represent the masses of PTFE and carbon in a unit volume of the porous domain. ω_{PTFE} denotes the weight loading, which was 5 wt% in this study. Figure 2B illustrates the generated random heterogeneous structure of GDLs with a porosity of 0.8. The carbon fibers were oriented layer by layer without overlapping, which led to anisotropic microstructures. The pore volume near fiber surfaces and the corner of two fibers in contact were filled with PTFE, which was clustered with a dark blue color, as shown in Figure 2B. Considering the properties of commercially available carbon fiber GDLs,[34,35] GDLs with the porosities ranging from 0.6 to 0.9 were generated for the current study.

2.2.3 | MPL modeling

The generation process of the MPL structure was divided into two main steps, namely, the generation of carbon particles and the addition of PTFE. The volume fractions of the carbon particles and PTFE were both determined according to Equations 2 to 4. In this study, all the carbon particles were presumed to be spheres with uniform diameters of 50 nm. In the first step, a small number of carbon spheres were randomly selected as seed particles in the MPL domain with a thickness of 5 μm. Next, the remaining spheres were added, which were adjacent to and connected with a minimum of one existing sphere, until the prescribed number of carbon particles was achieved. In the final step, the PTFEs were generated by filling the small pores between carbon particles until the required number was reached. MPLs were generated with porosity range from 0.3 to 0.6 in this work.[36] The three-dimensional structure of an MPL with a porosity of 0.6 is presented in Figure 2C. Carbon spheres were randomly distributed and attached to the PTFEs, as indicated by the dark blue color in the figure.

2.3 | Lattice Boltzmann method

The lattice Bhatnagar-Gross-Krook (LBGK) model[37] was employed to simulate the reactant flow transport phenomena within the porous media. In the LBM, transport characteristics, including the microscopic velocity, pressure, and density, are calculated by tracking the evolution of the particle distribution function, which is defined as the probability of a molecule at spatial position $\mathbf{x}$ at time t with momentum $\mathbf{p}$.[38] In this study, a single-phase LBM with a single relaxation time parameter T_r was used. The D3Q19 (ie, 3D 19-velocity) scheme is illustrated in Figure 3. The LBM consists of two main steps: collision and streaming. The evolution of the distribution function $f_a(\mathbf{x}, t)$ is as follows[39]:

$$\begin{aligned} f_a(\mathbf{x} + e_a \Delta t, t + \Delta t) &- f_a(\mathbf{x}, t) \\ &= -\frac{\Delta t}{T_r} \left(f_a(\mathbf{x}, t) - f_a^{\text{eq}}(\mathbf{x}, t) \right) \end{aligned} \quad (5)$$

where a is the lattice velocity index; $\mathbf{e}_a$ and Δt are the lattice velocities in the ath direction and unit time scale, respectively. T_r represents the relaxation time required to achieve the equilibrium distribution f_a^{eq}. A collision operator denotes the collision as a relaxation of the density distribution function toward the Maxwell-Boltzmann equilibrium distribution function.[39] In the D3Q19 scheme, the collision operator f_a^{eq} is the Maxwellian distribution function, which is expressed as[37]

$$f_a^{\text{eq}}(\mathbf{x}, t) = \omega_a \rho(\mathbf{x}, t) \left[1 + \frac{\mathbf{e}_a \mathbf{u}^{\text{eq}}}{c_s^2} + \frac{\mathbf{e}_a \mathbf{u}^{\text{eq}}}{2c_s^4} - \frac{(\mathbf{u}^{\text{eq}})^2}{2c_s^2} \right] \quad (6)$$

where ω_a is the weighting associated with the velocity $\mathbf{e}_a$, and it is defined for 19 components as follows:
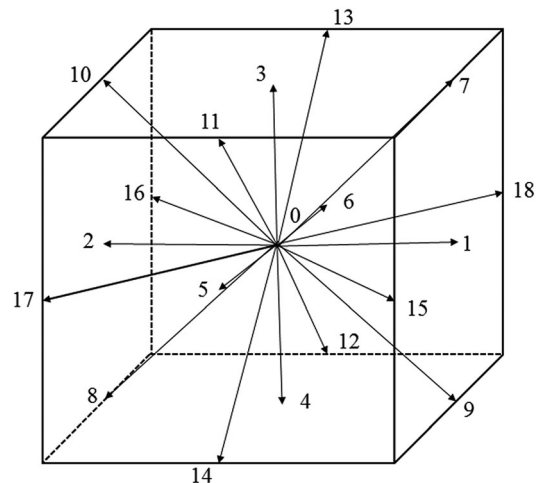

FIGURE 3 Lattice velocity directions of the D3Q19 LBM

$$\omega_a = \begin{cases} 1/3 & a = 0 \\ 1/18 & a = 1, \; 2, \; ..., \; 6 \\ 1/36 & a = 7, \; 8, \; ..., \; 18 \end{cases} \quad (7)$$

where c_s is the lattice sound velocity, which is equal to $1/\sqrt{3}$ for the D3Q19 model. The relationship between the kinematic viscosity ν and relaxation time is given by[37,40]

$$\nu = c_s^2 \left(\frac{T_r}{\Delta t} - \frac{1}{2} \right) \Delta t \quad (8)$$

$$\nu = \frac{2T_r - \Delta t}{6} \quad (9)$$

For the D3Q19 lattice model, $\mathbf{e}_a$ is expressed as

$$\mathbf{e}_a = c \times \begin{cases} (0, 0, 0) & a = 0 \\ (\pm 1, 0, 0), (0, \pm 1, 0), (0, 0, \pm 1) & a = 1, 2, ..., 6 \\ (\pm 1, \pm 1, 0), (\pm 1, 0, \pm 1), (0, \pm 1, \pm 1) & a = 7, \; 8, \; ..., \; 18 \end{cases} \quad (10)$$

where c represents the lattice speed $c = \Delta x / \Delta t$, which is set as unity (ie, $\Delta x = 1$, $\Delta t = 1$, and $c = 1$). The terms $\mathbf{u}^{eq}$ and ρ represent the macroscopic equilibrium velocity and the fluid density, respectively. The fluid density is calculated based on the conservation of the mass and momentum of the distribution function,

$$\rho = \sum_{a=0}^{18} f_a \quad (11)$$

$$\rho \mathbf{u}^{eq} = \sum_{a=0}^{18} \mathbf{e}_a f_a \quad (12)$$

Hence, the fluid velocity is expressed as

$$\mathbf{u}^{eq} = \frac{1}{\rho} \sum_{a=0}^{18} \mathbf{e}_a f_a \quad (13)$$

In this study, the physical unit properties were converted into lattice unit properties by matching the dimensionless characteristic parameters (ie, the Reynolds number). The Reynolds numbers in the lattice unit and physical unit were identical, and they were calculated as follows:

$$\text{Re} = \left. \frac{LU}{\nu} \right|_{Phys.} = \left. \frac{LU}{\nu} \right|_{Lattice} \quad (14)$$

where L and U are the characteristic length and fluid velocity, respectively.

Diffuse reflection potentially occurs when gas molecules collide with a solid wall, which implies that the gas molecules are reflected at random angles uncorrelated with the entry angles.[41] Therefore, a finite slip velocity u_w of the reactant gas, which is relative to the solid surfaces, may be used to balance the insufficiently low reflected tangential momentum. At a low Reynolds number, the slip velocity is expressed as follows[41]:

$$\frac{u_w}{U} \approx 0.4 \text{Kn} \sqrt{\text{Re}_x} \quad (15)$$

where $\text{Re}_x = Ux/\nu$ and x is the distance from the leading edge of the solid surface.

In this study, the inlet gas velocity (ie, intrinsic velocity through void space) of the composite porous media was set as 0.1 m/s. The viscosity of the reactant gas was 2.34×10^{-5} kg/m s, and the slip velocity at $x = 80$ μm (ie, the average pore radius in the channel) was calculated as

$$\frac{u_w}{U} \approx 0.4 \text{Kn} \sqrt{\text{Re}_x} = 4.79 \times 10^{-4} \quad (16)$$

This implies that the slip velocity of gas molecules at the gas-solid surface in this study was negligible and that a no-slip condition could be used to accurately determine the actual physical behavior of the fluid molecules. Consequently, the velocities at the inlet and outlet were solved using the standard deflection rule,[42] which assumes that any molecule that collides with a solid wall is deflected in its original direction with the same velocity.

2.4 | Determination of the trial number

For the statistical analysis in random structures, a sufficient number of sampling structures is needed to determine the statistical properties of the porous media. In this study, the sample size (ie, trial number) is chosen by using the confidence level. In probability theory, the confidence level refers to the percentage of all possible samples that are expected to include the actual population parameter (eg, initially predetermined porosity).[43,44] If the population approaches infinity, a cumulative normal distribution $P(\varphi)$ exists for φ based on the central limit theorem,[45] which is defined as follows:

$$P(\varphi) = \frac{1}{\sqrt{2\pi}\sigma_\varphi} \int_{-\infty}^{\varphi} e^{-\frac{(\varphi - m)^2}{2\sigma_\varphi^2}} d\varphi \quad (17)$$

where m presents the true mean of the random variable (eg, average volume fraction) and σ_φ is the standard deviation of φ. For a sufficiently large sample, a modified form of the de Moivre-Laplace limit theorem is

applied to describe a symmetric range centered on the mean[46]:

$$\alpha_k = \Pr\left[\left|\varphi^k - \overline{\varphi}^k\right| \geq \epsilon\right] \cong 2(k-1)\left[1 - P\left(\epsilon\sqrt{\frac{n}{\varphi^k(1-\varphi^k)}}\right)\right]$$

(18)

where k is the number of components. In metal foam channels, k is equal to 2; α^k is the rejection rate for the kth component; the error, ϵ, is accepted as 2×10^{-4} for this study; and n is the sample number.[46] φ^k and $\overline{\varphi}^k$ are the estimated and expected mean volume fractions, respectively. To achieve a 95% confidence level, which is the most commonly used in the statistical analysis,[30] the sum of the rejection rates for the kth component should correspond to 0.05. Here, if we take metal foam channels as an example, the related expressions are

$$\sum \alpha^k = \alpha^{pore} + \alpha^{metal} = 0.05$$

(19)

$$\sum \alpha^k = 2(k-1)\left[2 - \left\{P\left(\epsilon\sqrt{\frac{n}{\varphi^{pore}(1-\varphi^{pore})}}\right)\right.\right.$$
$$\left.\left. + P\left(\epsilon\sqrt{\frac{n}{\varphi^{metal}(1-\varphi^{metal})}}\right)\right\}\right]$$

(20)

For the worst-case scenario, the superficial volume fractions of the two components over the entire population domain are assumed as identical, and this leads to the following expressions:

$$\sum \alpha^k = 4(k-1)\left\{1 - \left[P\left(\epsilon\sqrt{\frac{n}{\varphi(1-\varphi)}}\right)\right]\right\} = 0.05$$

(21)

$$P\left(\epsilon\sqrt{\frac{n}{\varphi(1-\varphi)}}\right) \cong 0.9875$$

(22)

Consequently,

$$\epsilon\sqrt{\frac{n}{\varphi(1-\varphi)}} = 2.24$$

(23)

If we reconstruct the channels with a lattice grid of size $125 \times 125 \times 125$, the smallest number of required trials for each specified porosity for the statistical analysis is determined as follows:

$$N = \frac{\left(\frac{2.24}{0.0002}\right)^2 \times 0.5 \times (1-0.5)}{125 \times 125 \times 125} \approx 16$$

(24)

Based on the uncertainty of the random distributions of all the components in the domain, the number of trials required for each specific porosity is determined as 20 to increase the reliability. In the same way, the number of trials for each specific porosity of GDLs and MPLs is set as 15 and 30, respectively.

3 | RESULTS AND DISCUSSION

### 3.1 | Morphological structures of porous transport media

Figure 4 presents the superficial pore volume fractions for the metal-foam channels, porous GDLs, and MPLs with initial superficial porosities of 0.90, 0.80, and 0.30, which were used as a reference case in this study. As shown in Figure 4, the average pore volume fractions of the channel, GDL, and MPL were identical to the predetermined superficial pore volume fractions. It should be noted that the superficial pore volume fractions of three different trial sets of the reference channels, GDLs, and MPLs were approximately in accordance with the normal distributions, with standard deviations of 0.07%, 0.30%, and 0.10%, respectively. This demonstrates that 20, 15, and 30 trials were sufficient for the statistical analyses at a 95% confidence level, respectively.

Pore interconnections have a significant influence on the mass transport characteristics within porous media. At every point in the pore structures, a circle was inscribed with a radius equal to the minimum distance to the nearest wall. In this study, the pore size distributions of the three different porous media were predicted based on the microstructures and then determined with spheres of expanding radii. The pore size is defined as the largest spherical distance of a pore center to the solid phase.[47] Every nodal point of a pore corresponds to the center of a sphere, in which the radius extends to the edges of the solid sphere. The maximum radius of the
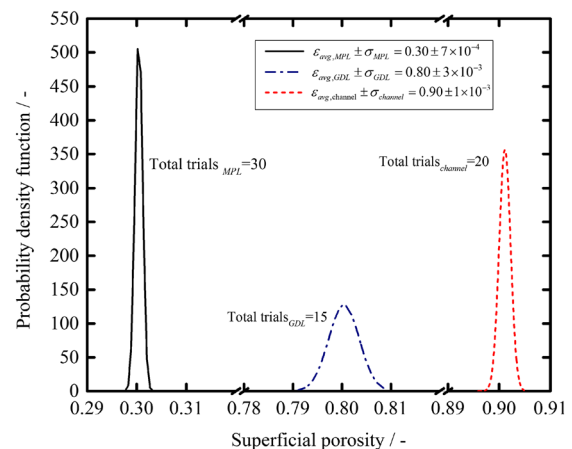
FIGURE 4 Normal distribution curve for structured superficial pore volume with a 95% confidence level [Colour figure can be viewed at wileyonlinelibrary.com]

sphere is considered as the pore radius at the grid point. Figure 5 presents three-dimensional cross-sectional views of the computed pore radii at local different sections for
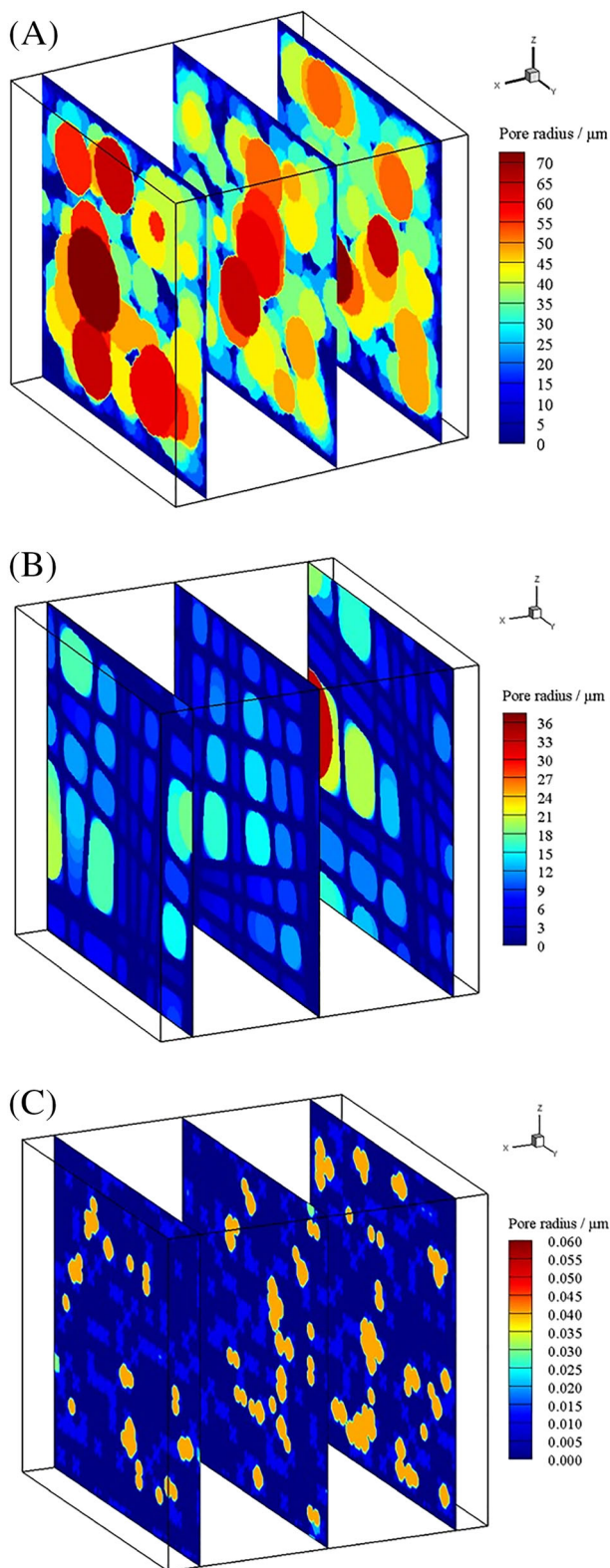
FIGURE 5 In-plane slices of pore size distribution contours of A, metal foam channel, B, GDL, and C, MPL [Colour figure can be viewed at wileyonlinelibrary.com]

the reference case, which exhibited heterogeneous structures with random pore interconnections. As shown in Figure 5A, the maximum pore radius at the three difference sections of the metal foam channel was calculated as 70 μm. The rectangular shapes of the void spaces presented in Figure 5B were generated by combining two adjacent carbon fiber layers. The maximum pore radius at the cross sections was calculated as 36 μm. In the reference MPL, as presented in Figure 5C, the generated carbon particles were randomly distributed and connected, where the maximum radius was 60 nm.

The pore diameter histogram from the numerical estimation was plotted, as shown in Figure 6. The estimated pore diameter curves were approximately in accordance with normal distributions. The highest frequencies of the MPLs, GDLs, and channels were 47%, 38%, and 29%, respectively, where the corresponding pore diameters were 0.40, 15, and 200 μm. The average, minimum, and maximum pore diameters of the reference MPL with a porosity of 0.30 were calculated as 0.042, 0.010, and 0.150 μm, respectively.

The condensation of water vapor may cause the formation of liquid water within GDLs. It is widely recognized that water transport in GDLs is highly dependent on the capillary pressure P_c and the pressure difference at the interface between wetting and nonwetting phases, which can be expressed as[2]

$$P_c = P_{nw} - P_w = \frac{2\gamma \cos\theta}{r_{pore}} \quad (25)$$

where r_{pore} is the pore radius. γ and $\cos\theta$ are the surface tension and a representative contact angle, respectively. Moreover, GDLs are typically treated with hydrophobic PTFEs and therefore require combined (ie, hydrophobic and hydrophilic) pore-size distribution analyses. Some pores may attract water, whereas other pores may repel water because of the heterogeneous structures in the
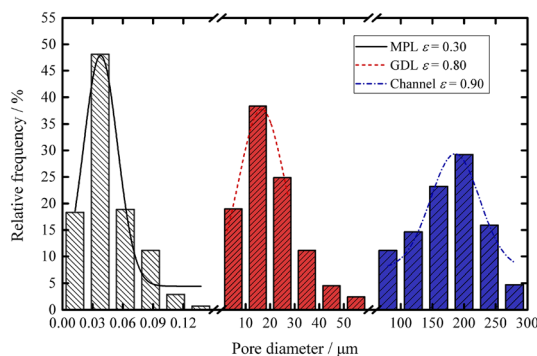
FIGURE 6 Histograms of the computed pore size distribution in channels, GDLs, and MPLs [Colour figure can be viewed at wileyonlinelibrary.com]

GDLs. Hence, water may be in either the wetting or nonwetting phase. Kumbur et al established a modified Leverett function, in addition to several parallel functions, to describe the capillary pressure for GDLs with various PTFE contents ranging from 0 to 20 wt%,[48-50] in which the P_c for the hydrophobic pores is defined as

$$P_c = \gamma \cos\theta \left(\frac{\varepsilon}{\kappa}\right)^{1/2} M(s_{nw}) \tag{26}$$

where κ represents the permeability of the nonwetting phase. $M(s_{nw})$ represents the empirical Leverett function[51] related to the PTFE content wt% and liquid saturation s_{nw}. The critical radius for the hydrophobic pores r_{HO} can be derived by combining Equations 25 and 26 as follows:

$$r_{HO} = \frac{2}{M(s_{nw})} \left(\frac{\kappa}{\varepsilon}\right)^{\frac{1}{2}} \tag{27}$$

where $\kappa = 1 \times 10^{-12} \text{m}^2$ for liquid water.[52] In this study, $f_{r_{pore}>r_{HO}}$ was used to represent the fraction of pores with sizes larger than r_{HO} in GDLs, and it is defined as

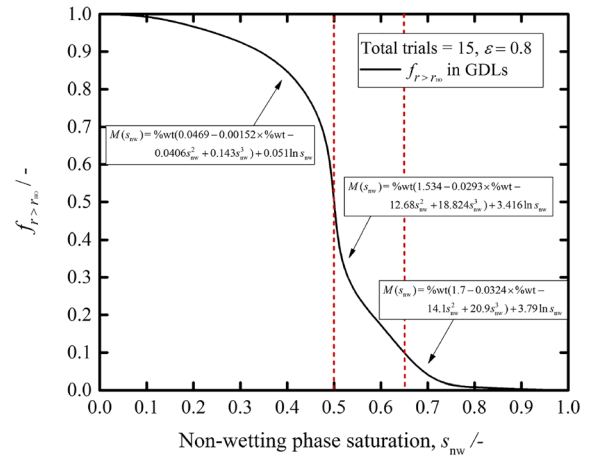$$f_{r_{pore}>r_{HO}} = \frac{\text{number of pores with } r_{pore} > r_{HO}}{\text{total pore number}} \tag{28}$$

Figure 7 presents the relationship between $f_{r>r_{HO}}$ and the nonwetting phase saturation s_{nw} in the GDLs. It should be noted that water is the nonwetting phase in hydrophobic pores. The overall nonwetting saturation domain is divided into three regions: $0 < s_{nw} < 0.5$ (low hydrophobic region), $0.5 \leq s_{nw} \leq 0.65$ (transition region), and $0.65 < s_{nw} < 1$ (high capillary region) with three parallel functions of $M(s_{nw})$, as shown in Figure 7.[51]


FIGURE 7 Relationship between hydrophobic pore fraction and nonwetting phase saturation in mixed wettability GDLs [Colour figure can be viewed at wileyonlinelibrary.com]

presents the computed velocity vectors throughout the reference 0.4-mm-thick channel and 200-µm-thick GDL with a maximum local velocity of 0.5 m/s. As can be seen, it is more favorable for fluid flow to pass through large pores rather than small pores, because of the lower flow resistance of larger pores. The tortuous streaklines in the composite porous media correspond to the velocity vectors were obtained from the positions of all the fluid particles that continuously pass through the channel entrance. The shape of the streaklines, which were parallel to the local velocity vector, was used to calculate the tortuosity τ of the porous media as follows[53,54]:

$$M(s_{nw}) = \begin{cases} \%\text{wt}\left(0.0469 - 0.00152 \times \%\text{wt} - 0.0406s_{nw}^2 + 0.143s_{nw}^3\right) + 0.051\ln s_{nw} & 0 < s_{nw} < 0.5 \\ \%\text{wt}\left(1.534 - 0.0293 \times \%\text{wt} - 12.68s_{nw}^2 + 18.824s_{nw}^3\right) + 3.416\ln s_{nw} & 0.5 \leq s_{nw} \leq 0.65 \\ \%\text{wt}\left(1.7 - 0.0324 \times \%\text{wt} - 14.1s_{nw}^2 + 20.9s_{nw}^3\right) + 3.79\ln s_{nw}, & 0.65 < s_{nw} < 1 \end{cases} \tag{29}$$

Moreover, $f_{r>r_{HO}}$ decreases in a sinusoidal manner as the water saturation increases from 0 to 1. Water flooding may occur in the GDLs with s_{nw} close to 1, in which water accumulates and converts to the wetting phase.

3.2 | Heterogeneous mass transport properties

In this study, it was assumed that the inlet velocity at the entrance of the channels was set as 0.1 m/s. Figure 8A

$$\tau = \left(\frac{l_{real}}{l}\right)^2 = \left(\frac{\sum u(r)}{\sum u_x}\right)^2 \tag{30}$$

where l_{real} is the average real path length of the fluid flow through interconnected pores and l is the minimum available length (ie, the physical thickness of the porous media). $u(r)$ represents the tangential velocity of the streakline starting at point r, and u_x is its component in the x-direction. The relationships between the porosity
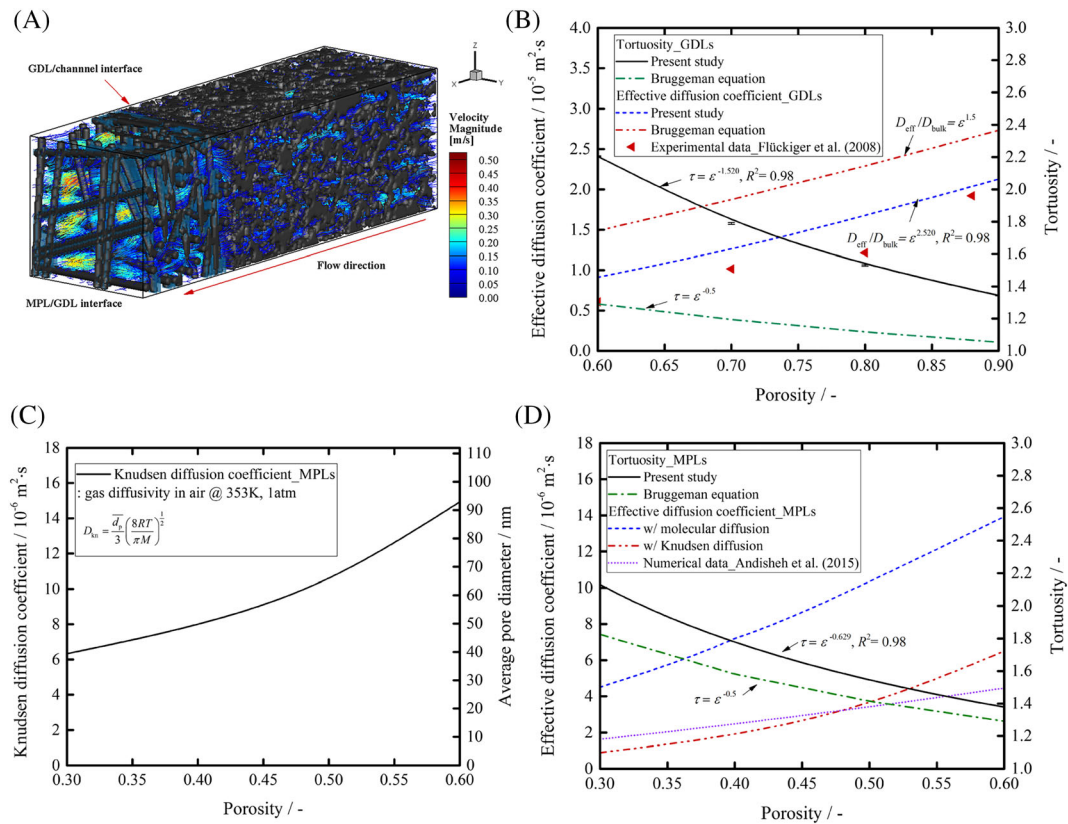
FIGURE 8 A, Computed 3D velocity vector and streakline distribution in the reference GDL and channel. B, Relationship between porosity and tortuosity in the principal direction and the variation in the effective diffusivity as a function of porosity in the GDLs. C, Variation of Knudsen diffusion coefficient in MPLs as a function of porosity. D, Relationship between porosity and tortuosity in the principal direction and statistical comparison of the effective diffusivity obtained in this study and other group [Colour figure can be viewed at wileyonlinelibrary.com]

and the statistically estimated average through-plane (ie, principle flow direction) tortuosities of the GDLs and MPLs in the porosity ranges of 0.6 to 0.9 and 0.3 to 0.6, respectively, were compared with the classic Bruggeman correlation[53,54]

$$\tau = \varepsilon^{\alpha} = \varepsilon^{-0.5} \tag{31}$$

The exponent α for the GDLs and MPLs was fitted with −1.520 and −0.629, respectively. The numerical predictions reveal that the Bruggeman equation underestimated the tortuosities of the GDLs and MPLs, as depicted in Figure 8B and 8C, respectively, and should be modified with a lower exponent α for PEFC applications.

In random porous media, intergas collisions and the collisions between gas molecules and the pore wall occur frequently because of the heterogeneous structures. The Knudsen number was employed to approximately determine the mass diffusion mechanism, which is defined as the ratio of the mean free path of gas molecules λ to the pore diameter. The molecular mean free path was estimated as follows[55-57]:

$$\lambda = \frac{k_B T}{\sqrt{2}\pi d_m^2 P} \tag{32}$$

where k_B is the Boltzmann constant (1.381×10^{-23} J/K), T is the gas temperature (K), d_m is the molecular diameter of the fluid, and P denotes the pressure (Pa). According to Equation 32, for a particle diameter of 3 Å at 353 K and 1 atm, the mean free path of the fluid was approximately 120 nm. It is suggested that when the pore diameter of porous media is comparable with or smaller than the mean free path, fluid molecules collide more frequently with solid surfaces, and the Knudsen effect should be considered. On the contrary, for pore diameters that are significantly larger than the mean free path, Knudsen diffusion is negligible, and the collisions and interactions between gas molecules are dominant.[58] The estimated results from the previous section, as shown in Figure 6, imply that the average pore diameter of the GDLs exceeds the mean free path length of the reactant gas ($\lambda \approx 120$ nm). Hence, the collisions between the reactant gas molecules and the solid surfaces are negligible. The mass diffusion phenomena within the GDLs are

associated with the heterogeneous morphological pore structures, in which pores with various diameters are randomly distributed and tortuous interconnections are formed. Consequently, the mass diffusion coefficient D of the GDLs was modified by the porosity and tortuosity as follows[53,54]:

$$D_{\text{eff}} = \frac{\varepsilon}{\tau}D \tag{33}$$

Figure 8B presents the variation in the average effective mass diffusion coefficient as a function of the porosity and the tortuosity in the GDLs as follows:

$$D_{\text{eff}} = \frac{\varepsilon}{\varepsilon^{-1.520}}D = \varepsilon^{2.520}D \tag{34}$$

with $R^2 = 0.98$, where D_{eff} is the effective mass diffusion coefficient. The molecular diffusion of the fluid was assumed to be 3.2×10^{-5} m^2/s. The evaluated effective diffusivity of the reactant gas in the cathode continuously increased from 9.12×10^{-6} to 2.13×10^{-5} m^2/s as the porosity was varied from 0.6 to 0.9. A set of experimental data[13] was marked in Figure 8B, which indicates that Equation (34) derived in this study was significantly closer to the experimental data than the typical Bruggeman correlation,[59] which overestimated the effective diffusivity resulting from the lower prediction of the tortuosity, as previously discussed.

According to the estimated pore diameters, the average pore diameter in the MPLs was 92.7 nm, which was smaller than the mean free path length of 120 nm. Consequently, the Knudsen effect on the effective transport mechanism should be considered. The Knudsen diffusion coefficient of the fluid can be evaluated as follows[60]:

$$D_{\text{kn}} = \frac{\overline{d_{\text{p}}}}{3}\left(\frac{8RT}{\pi M}\right)^{\frac{1}{2}} \tag{35}$$

where $\overline{d}_{\text{P}}$ represents the average pore diameter. R is the gas constant (8.314 J/mol K), and M is the molecular mass of the reactant gas. Figure 8C presents the estimated Knudsen diffusion coefficient calculated from the corresponding average pore diameter of 30 reference MPLs. The Knudsen diffusion coefficient increased from 6.33×10^{-6} to 1.49×10^{-5} m^2/s as the average pore diameter extended from 39.3 to 92.7 nm in the porosity range of 0.3 to 0.6.

Figure 8D presents the effective diffusion coefficient of the MPLs, which was investigated in the porosity range of 0.3 to 0.6. Moreover, the molecular diffusion and Knudsen diffusion were considered as the diffusion mechanism. Numerical estimations from another research group[61] were plotted, as shown in Figure 8D, for comparison. A significant discrepancy between the two

numerical estimations of the effective diffusion coefficients was observed when considering molecular diffusion as the dominant diffusion mechanism within MPLs, which indicates that molecular diffusion is not the dominant mass diffusion mechanism. Conversely, the average effective diffusion coefficient was in good agreement with the numerical predictions from the other research group when considering Knudsen diffusion as the dominant diffusion mechanism. The average effective diffusion coefficient increased from 8.92×10^{-7} to 6.5×10^{-6} m^2/s as the porosity increased from 0.3 to 0.6.

The permeability κ is a critical physical property that affects the mass transportation performance in the heterogeneous porous media. The permeability κ of a porous medium under the low Reynolds number condition is defined by Darcy's law[62] as

$$\overline{\mathbf{u}} = -\frac{\kappa}{\mu}\nabla p \tag{36}$$

where $\overline{\mathbf{u}}$ represents the volume-averaged velocity through the porous medium, μ is the viscosity of the fluid flow, and ∇p is the pressure gradient vector. In the porous media, the pressure gradient is related to the through- and in-plane lengths of the fluid flow and the difference between the inlet and outlet pressures. Permeability of porous media is usually described as a function of physical properties (eg, porosity).[63] In this study, the in-plane and through-plane permeabilities were calculated from the flow field properties obtained from the LBM simulation. Figure 9 presents the estimated correlations between the permeabilities of the reactant gases and porosities of the channels, GDLs, and MPLs, respectively. The average permeabilities of three porous media were predicted from sets of trials for each case, for the statistical analysis. As seen in Figure 9A, the average through- and in-plane permeabilities in the porosity range of 0.80 to 0.95 of the metal foam channels successively increased from 8.17×10^{-8} to 1.32×10^{-7} m^2/s and from 8.22×10^{-8} to 1.31×10^{-7} m^2/s, respectively. The calculated permeabilities were mathematically approximated in polynomial forms as follows:

$$\kappa_{\text{TP\_channel}} = 5.707 \times 10^{-7}\varepsilon^2 - 6.683 \times 10^{-7}\varepsilon + 2.515 \times 10^{-7} \tag{37}$$

$$\kappa_{\text{IP\_channel}} = 3.022 \times 10^{-7}\varepsilon^2 - 2.071 \times 10^{-7}\varepsilon + 5.479 \times 10^{-8} \tag{38}$$

where $R^2 = 0.99$. The simulation results reveal that the through- and in-plane permeabilities of the channels approximately coincided because of the isotropic porous
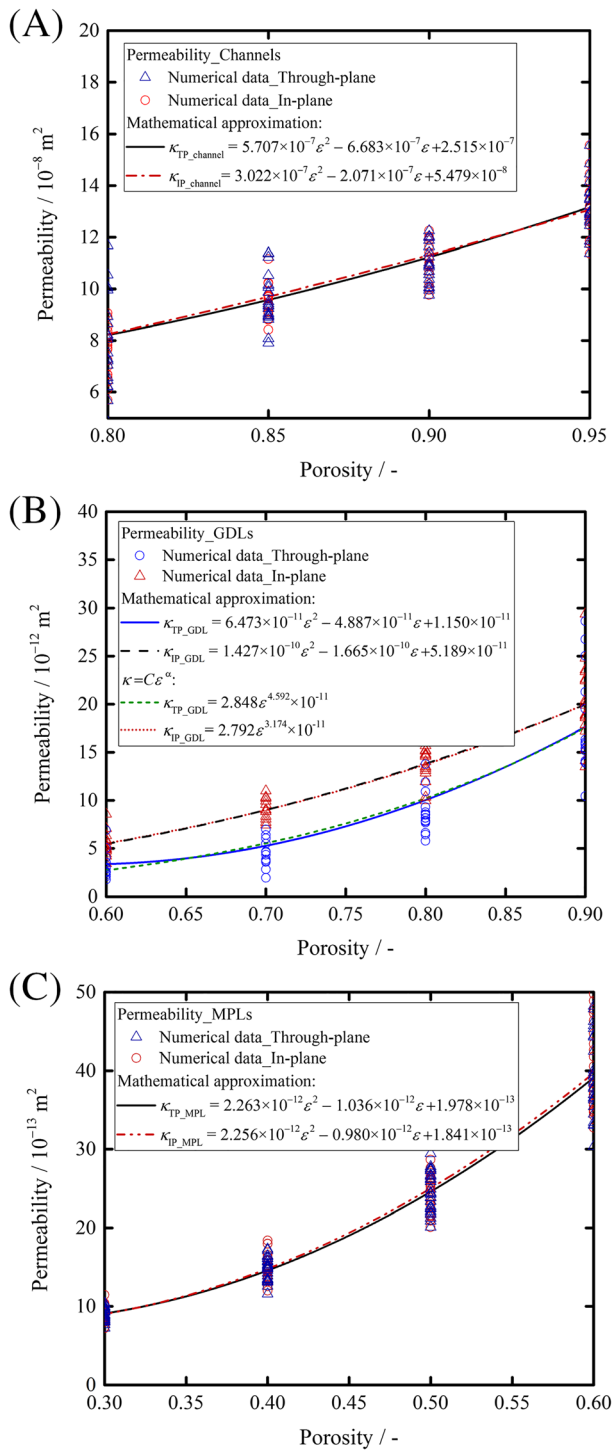
FIGURE 9 Statistically estimated relationship between porosity and through- and in-plane permeabilities in the A, channels, B, GDLs, and C, MPLs [Colour figure can be viewed at wileyonlinelibrary.com]

structures of the metal foam channels. Paek et al[5] measured the permeability of aluminum metal foam with a porosity of 0.92 and reported a permeability range from 0.75×10^{-7} to $2.4 \times 10^{-7} m^2$. In this study, the estimated metal foam permeability for $\varepsilon = 0.92$ is 1.19×10^{-7} and $1.42 \times 10^{-7} m^2$ in through- and in-plane directions,

respectively, demonstrating a good agreement with the experimental results reported by Paek et al.[5]

The average through- and in-plane permeabilities of the GDLs were estimated from a set of 15 references for each case, as established in Figure 9B. The calculated average through-plane permeability continuously extended from 3.17×10^{-11} to 1.78×10^{-10} m^2, whereas the in-plane permeability steadily increased from 5.36×10^{-11} to 2.00×10^{-10} m^2. The predicted permeabilities were fit as follows:

$$\kappa_{TP\_GDL} = 6.473 \times 10^{-11}\varepsilon^2 - 4.887 \times 10^{-11}\varepsilon + 1.150 \times 10^{-11} \tag{39}$$

$$\kappa_{IP\_GDL} = 1.427 \times 10^{-10}\varepsilon^2 - 1.665 \times 10^{-10}\varepsilon + 5.189 \times 10^{-11} \tag{40}$$

where $R^2 = 0.99$. The Kozeny-Carman equation[6] is commonly used to predict the permeabilities of porous media. However, it was originally intended for the packed bed geometry with spherical particles, and it is only applicable to materials with low porosities, which may not predict the permeability accurately. Thus, it is not presented in this paper. Moreover, a general empirical expression was used for GDL structures with PTFE[15,64]:

$$\kappa = C\varepsilon^{\alpha} \tag{41}$$

where C is a constant. As seen in Figure 9B, $C = 2.848 \times 10^{-10}$ and $\alpha = 4.592$ were fit for the through-plane permeability, whereas $C = 2.792 \times 10^{-10}$ and $\alpha = 3.174$ were fit for the simulated in-plane permeability. It was found that the in-plane permeability always exceeds the through-plane permeability because of the anisotropic structures of the GDLs. This indicates that the alignment of fibers in the in-plane results in a lesser flow resistance along the fibers than to that normal to the fibers. The through- and in-plane permeabilities of SGL 24BA GDL, which has a thickness approximately 200 μm with a porosity of 0.84,[65] was measured as 1.45×10^{-11} and $1.56 \times 10^{-11} m^2$, respectively, by Gostick et al.[7] According to the results of this study, when the porosity is 0.84, the predicted though- and in-plane permeabilities are 1.27×10^{-11} and $1.60 \times 10^{-11} m^2$, respectively, which are comparable with the experiment results.[7]

The average through- and in-plane permeabilities of 30 reference MPLs are presented in Figure 9B, which were approximated as follows:

$$\kappa_{TP\_MPL} = 2.263 \times 10^{-12}\varepsilon^2 - 1.036 \times 10^{-12}\varepsilon + 1.978 \times 10^{-13} \tag{42}$$

$$\kappa_{IP\_MPL} = 2.256 \times 10^{-12}\varepsilon^2 - 0.980 \times 10^{-12}\varepsilon + 1.841 \times 10^{-13} \tag{43}$$

where $R^2 = 0.99$. The two permeabilities were found to coincide in the porosity range of 0.3 to 0.6, which indicates that the MPLs contain isotropic porous structures. The MPL permeability increased from 0.90×10^{-13} to $3.90 \times 10^{-13} m^2$ when the porosity increased from 0.3 to 0.6. The predicted MPL permeability values are found with two orders of magnitude less than the GDL permeability and have a good agreement with the experimental results reported by Pant et al.[66] They measured two SGL 34BC GDL-MPL assemblies and calculated the MPL permeability with values 1.31×10^{-13} and $1.39 \times 10^{-13} m^2$. Additionally, compared with the metal foam channels and GDLs, the MPLs exhibited the smallest permeability among the three porous transport media. This may be because of the low porosities and small pore sizes, which resulted in a high fluid flow resistance.

3.3 | Interfacial contact properties

The interface between the different layers of porous media can have a considerable effect on the multitransport performance of fuel cells. In order to investigate interfacial contact properties between porous media, local porosity was calculated as an index of the pore size distribution at the interface. The local porosity of a certain porous surface is defined as[67]

$$\varepsilon_x = \frac{1}{V_l} \int_V a(x) \, dV = \frac{V_l^{po}}{V_l} \quad (44)$$

where V_l is the smallest differential volume that results in a statistically significant local porosity. V_l^{po} represents the volume occupied by the void or fluid. $a(x)$ is a void distribution function, and it is determined as follows:

$$a(x) = \begin{cases} 1 & \text{if } x \text{ is the void region} \\ 0 & \text{if } x \text{ is the solid region.} \end{cases} \quad (45)$$

The interfacial contact areal ratio $f_{M/N,C_M}$ of media M with adjacent media N is defined as

$$f_{M/N,C_M} = \frac{A_{M/N,C}}{A_M} \quad (46)$$

in which $A_{M/N, C}$ is the contact solid area of media M and N at the interface M/N, and A_M is the total solid area occupied by M at the interface. In this study, the interfacial areal contact ratios at the channel/GDL and GDL/MPL interfaces were estimated for a wide range of local porosities without compression.

As shown in Figure 10A, at channel/GDL interfaces, with a fixed channel local porosity of 0.9 (ie, $\varepsilon_{L, CH}$), the average interfacial areal contact ratio of channels steadily reduced from 0.37 to 0.08 as the local porosity of GDL (ie,
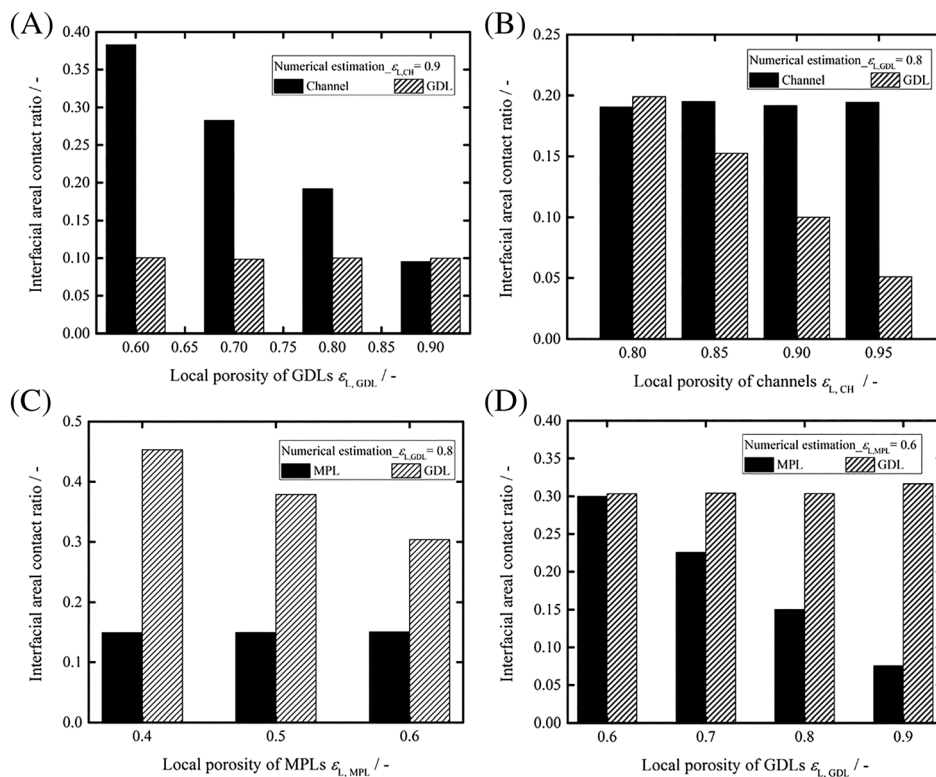
FIGURE 10 Interfacial areal contact ratio of A, MPL and B, GDL at GDL/MPL interface and C, GDL and D, metal foam channel at GDL/channel interface

$\varepsilon_{L, GDL}$) varied from 0.6 to 0.9. However, for the GDL, there was a negligible variation in the average interfacial areal contact ratio for the same numerical case. Conversely, when $\varepsilon_{L, GDL}$ was set as 0.8, as shown in Figure 10B, no significant changes were observed in the interfacial areal contact ratio of the GDLs. By contrast, the average interfacial areal contact ratio of the channels decreased from 0.20 to 0.05.

Furthermore, Figure 10C and 10D presents the variations in the interfacial areal contact ratio at GDL/MPL interfaces. As shown in Figure 10C, when $\varepsilon_{L, GDL} = 0.8$, the areal contact ratio of the GDLs decreased from 0.45 to 0.3 in the local porosity of the MPL (ie, $\varepsilon_{L, MPL}$) range from 0.4 to 0.6, because of a decrease in the number of MPL carbon particles at the GDL/MPL interfaces. Similarly, the average areal contact ratio of the MPLs with a local porosity of 0.6 decreased from 0.3 to 0.07 in the GDL local porosity range of 0.6 to 0.9. However, no significant changes were observed in the average interfacial areal contact ratio of the GDLs in the same GDL local porosity range. The MPL carbon particles were measured in nanometers, and they were more uniformly distributed than carbon fibers in GDLs, which were measured in micrometers and directionally generated at the GDL/MPL interfaces. Hence, the contact area of the MPLs was significantly affected by the local porosity of the GDLs. Consequently, Figure 10 reveals that the variation in the local porosity of one porous medium has a significant influence on the interfacial areal contact ratio of its adjacent porous media with a fixed local porosity. It should be noted that the interfacial contact areal ratio is a critical property at the interface of adjacent porous transport media. High contact areal ratios at the interface can enhance the efficiency of thermal and electrical conductions. Pore interconnections related to reactant gas transport can be reduced by low local porosities at the interface. It is therefore essential to study the interfacial contact properties associated with the performance of fuel cells.

4 | CONCLUSIONS

A numerical study of the mass transport characteristics was conducted on heterogenous porous media at a 95% confidence level. Series of channels, GDLs, and MPLs were generated using the stochastic method considering different porosities and random structures, respectively, ie, the critical hydrophobic pore radius in the mixed wettability GDLs. The D3Q19 three-dimensional LBM was able to simulate the mass transport phenomena within a series of channels, GDLs, and MPLs, respectively. The hydrophobic pore distribution related to water condensation in the mixed wettability GDLs was estimated using a modified Leverett function. The fraction of pores with sizes larger than the critical hydrophobic pore radius decreases in a sinusoidal manner as the water saturation increases from 0 to 1 in GDLs. Microscale/nanoscale LBM transport modeling showed that the calculated through- and in-plane permeabilities approximately coincided in the channels and MPLs, respectively, because of the isotropic porous structures of the metal foam channels and MPLs. However, the in-plane permeability always exceeds the through-plane permeability in the GDLs, because of the anisotropic fiber alignments. Smaller exponents were applied to the statistically estimated tortuosities of the GDLs and MPLs than those applied to the classic Bruggeman equation. The average effective diffusion coefficients of the gas in the GDLs were estimated with a pre-estimated tortuosity, thus yielding a closer prediction to the experimental data from the literature than that of the typical Bruggeman correlation. The preestimated Knudsen diffusion coefficient and tortuosity were applied to predict the average effective diffusion coefficients of gas in the MPLs, which was in good agreement with the numerical effective diffusion coefficient data obtained by another research group. Moreover, the interfacial areal contact ratio between two adjacent porous media was estimated, and it was found to be significantly dependent on the local porosity of every porous medium at the interface. The present model and results are expected to contribute to the predictions of heterogeneous transport properties in the porous media.

COMPETING INTEREST

There are no competing interest to declare.

ORCID

Sukkee Um https://orcid.org/0000-0002-8017-5147

REFERENCES

1. Yuan W, Tang Y, Yang X, Wan Z. Porous metal materials for polymer electrolyte membrane fuel cells—a review. *Appl Energy*. 2012;94:309-329.

2. Mench MM. *Fuel Cell Engines*. New Jersey: John Wiley & Sons; 2008 292 p.

3. Kumar A, Reddy RG. Modeling of polymer electrolyte membrane fuel cell with metal foam in the gas flow-field of bipolar/end plates. *J Power Sources*. 2003;114(1):54-62.

4. Tsai BT, Tseng CJ, Liu ZS, Wang CH, Lee CI, Yang CC et al. Effects of flow field design on the performance of a PEM fuel cell with metal foam as the flow distributor. *Int J Hydrogen Energy*. 2012;37(17):13060-13066.

5. Paek JW, Kang BH, Kim SY, Hyun JM. Effective thermal conductivity and permeability of aluminum foam materials. *Int J Thermophys*. 2000;21(2):453-464.

6. Feser J, Prasad A, Advani S. Experimental characterization of in-plane permeability of gas diffusion layers. *J Power Sources*. 2006;162(2):1226-1231.

7. Gostick JT, Fowler MW, Pritzker MD, Ioannidis MA, Behra LM. In-plane and through-plane gas permeability of carbon fiber electrode backing layers. *J Power Sources*. 2006;162:228-238.

8. Kramer D, Freunberger SA, Flückiger R, et al. Electrochemical diffusimetry of fuel cell gas diffusion layers. *J Electroanal Chem*. 2008;612:63-77.

9. Flückiger R, Freunberger SA, Kramer D, Wokaun A, Scherer GG, Büchi FN. Anisotropic effective diffusivity of porous gas diffusion layer materials for PEFC. *Electrochim Acta*. 2008;54:551-559.

10. Zamel N, Astrath NGC, Li X, et al. Experimental determination of effective diffusion coefficient of oxygen-nitrogen mixture in carbon paper. *Chem Eng Sci*. 2010;65(2):931-937.

11. Baker D, Wieser C, Neyerlin KC, Murphy MW. The use of limiting current to determine transport resistance in PEM fuel cells. *ECS Transactions*. 2006;3:989-999.

12. Hwang G, Weber A. Effective-diffusivity measurement of partially-saturated fuel-cell gas-diffusion layers. *J Electrochem Soc*. 2012;159(11):F683-F692.

13. Ihonen J, Mikkola M, Lindbergh G. Flooding of gas diffusion backing in PEFCs: physical and electrochemical characterization. *J Electrochem Soc*. 2004;151(8):A1152-A1161.

14. Williams MV, Begg E, Bonville L, Hunz R, Fentona JM. Characterization of gas diffusion layers for PEMFC. *J Electrochem Soc*. 2004;151(8):A1173-a1180.

15. LaManna JM, Kandlikar SG. Determination of effective water vapour diffusion coefficient in PEMFC gas diffusion layers. *Int J Hydrogen Energy*. 2011;36(8):5021-5029.

16. Beugre D, Calvo S, Dethier G, Crine M, Toye D, Marchot P. Lattice Boltzmann 3D flow simulations on a metallic foam. *J Comput Appl Math*. 2010;234(7):2128-2134.

17. Park J, Matsubara M, Li X. Application of lattice Boltzmann method to a micro-scale flow simulation in the porous electrode of a PEM fuel cell. *J Power Sources*. 2007;173:404-414.

18. Wu W, Jiang F. Microstructure reconstruction and characterization of PEMFC electrodes. *Int J Hydrogen Energy*. 2014;39:15894-15906.

19. Ostadi H, Rama P, Liu Y, Chen R, Zhang XX, Jiang K. 3D reconstruction of a gas diffusion layer and a microporous layer. *J Memb Sci*. 2010;351:69-74.

20. Hao L, Cheng P. Lattice Boltzmann simulations of anisotropic permeabilities in carbon paper gas diffusion layers. *J Power Sources*. 2009;186:104-114.

21. Froning D, Yu J, Gaiselmann G, et al. Impact of compression on gas transport in non-woven gas diffusion layers of high temperature polymer electrolyte fuel cells. *J Power Sources*. 2016;318:26-34.

22. Espinoza M, Andersson M, Sundén B. Comparing through-plane diffusibility correlations in PEFC gas diffusion layers using the lattice Boltzmann method. *Int J Hydrogen Energy*. 2017;42(16):11689-11698.

23. You L, Liu H. A two-phase flow and transport model for the cathode of PEM fuel cells. *Int J Heat Mass Transfer*. 2002;45:2277-2287.

24. Lai X, Liu D, Peng L, Ni J. A mechanical–electrical finite element method model for predicting contact resistance between bipolar plate and gas diffusion layer in PEM fuel cells. *J Power Sources*. 2008;182(1):153-159.

25. Khandelwal M, Mench MM. Direct measurement of through-plane thermal conductivity and contact resistance in fuel cell materials. *J Power Sources*. 2006;161:1106-1115.

26. Makharia R, Mathias MF, Baker DR. Measurement of catalyst layer electrolyte resistance in PEFCs using electrochemical impedance spectroscopy. *J Electrochem Soc*. 2005;152:A970-A977.

27. Zhou P, Wu CW, Ma GJ. Contact resistance prediction and structure optimization of bipolar plates. *J Power Sources*. 2006;159:1115-1122.

28. Schweiss R, Meiser C, Damjanovic T, Galbiati I, Haak N. SIGRACET® gas diffusion layers for PEM fuel cells, electrolyzers and batteries. *White Pap SGL Group*. 2016;4-8.

29. Becker J, Flückiger R, Reum M, Büchi FN, Marone F, Stampanoni M. Determination of material properties of gas diffusion layers: experiments and simulations using phase contrast tomographic microscopy. *J Electrochem Soc*. 2009;156(10):B1175-B1181.

30. Zar JH. *Biostatistical Analysis*. 4th ed. Upper Saddle River, New Jersey: Prentice Hall; 1996:43-45.

31. Shin S, Kim AR, Um S. Statistical prediction of fuel cell catalyst effectiveness: quasi-random nano-structural analysis of carbon sphere-supported platinum catalysts. *Int J Hydrogen Energy*. 2016;41(22):9507-9520.

32. John B. Manufacturing routes for metallic foams, JOM. *Minerals, Metals & Materials Society*. 2000;52(12):22-27.

33. Simona C, Kartouziana D, Müller D, Wilhelm F, Gasteiger HA. Impact of microporous layer pore properties on liquid water transport in PEM fuel cells: carbon black type and perforation. *J Electrochem Soc*. 2017;164(14):F1697-F1711.

34. EI-kharouf A, Mason TJ, Brett DJL, Pollet BG. Ex-situ characterisation of gas diffusion layers for proton exchange membrane fuel cells. *J Power Sources*. 2012;218:393-404.

35. Thomas A, Maranzana G, Didierjean S, Dillet J, Lottin O. Thermal and water transfer in PEMFCs: investigating the role of the microporous layer. *International J of Hydrogen Energy*. 2014;39(6):2649-2658.

36. Becker J, Wieser C, Fell S, Steiner K. A multi-scale approach to material modeling of fuel cell diffusion media. *Int J Heat Mass Transfer*. 2011;54:1360-1368.

37. Guo Z, Shu C. Advances in computational fluid dynamics: Vol.3. In: *Lattice Boltzmann Method and its Applications in Engineering Chapter 1*. World Scientific; 2013.

38. Cekmer O, Um S, Mench MM. A combined path-percolation lattice–Boltzmann model applied to multiphase mass transfer in porous media. *Int J Heat Mass Transfer*. 2016;93:257-272.

39. Han B, Ni M, Meng H. Three-dimensional lattice Boltzmann simulation of liquid water transport in porous layer of PEMFC. *J Entropy*. 2016;18:17.

40. Mohamad AA. *Lattice Boltzmann method: fundamentals and engineering applications with computer codes*. London: Springer Science & Business Media; 2011.

41. White F. *Viscous fluid flow*. New York: McGraw-Hill; 1991:48.

42. Su H, Xu Q, Chong J, Li H, Sita C. Elimination micro-porous layer from gas diffusion electrode for use in high temperature polymer electrolyte membrane fuel cell. *J Power Sources*. 2017;341:302-308.

43. Cox DR, Hinkley DV. *Theoretical Statistics*. Chapman & Hall; 1974.

44. Kendall MG, Stuart DG. *The Advanced Theory of Statistics, Vol 2: Inference and Relationship*. London: Griffi; 1973.

45. Drake WA. *Fundamentals of applied probability theory*. New York: McGraw Hill; 2007.

46. Mavridis D, Aitken CG. Sample size determination for categorical responses. *J Forensic Sci*. 2009;54(1):135-151.

47. Bear J. *Dynamics of Fluids in Porous Media*. New York: Courier Corporation; 2013.

48. Udell KS. Heat transfer in porous media considering phase change and capillarity—the heat pipe effect. *Int J Heat Mass Transfer*. 1985;28:485-495.

49. Leverett MC. Capillary behavior in porous solids. *Am Inst Mining Met Eng Petroleum Dev Technol*. 1994;142:152.

50. Kumbar EC, Sharp KV, Mench MM. A validated Leverett approach to multiphase flow in polymer electrolyte fuel cell diffusion media: part 3, temperature effect and unified approach. *J Electrochem Soc*. 2007;154(12):B1315-B1324.

51. Kumbar EC, Sharp KV, Mench MM. A validated Leverett approach to multiphase flow in polymer electrolyte fuel cell diffusion media: part 1, hydrophobicity effect. *J Electrochem Soc*. 2007;154(12):B1295-B1304.

52. Holzer L, Pecho O, Schumacher J, et al. Microstructure-property relationships in a gas diffusion layer (GDL) for polymer electrolyte fuel cells, part II: pressure-induced water injection and liquid permeability. *Electrochim Acta*. 2017;241:414-432.

53. Wang Y, Cho S, Thiedmann R, Schmidt V, Lehnert W, Feng X. Stochastic modeling and direct simulation of the diffusion media for polymer electrolyte fuel cells. *Int J Heat Mass Transfer*. 2010;53:1128-1138.

54. Litster S, Epting W, Wargo E, Kalidindi S, Kumbur E. Morphological analyses of polymer electrolyte fuel cell electrodes with nano-scale computed tomography imaging. *Fuel Cells* 201. 13:935-945.

55. Hirschfelder JO, Curtiss RB. *Molecular Theory of Gases and Liquids*. New York: John Wiley; 1954.

56. He W, Lv W, Dickerson JH. *Gas Transport in Solid Oxide Fuel Cells*. London: Springer; 2014.

57. Welty JR, Wicks CE, Rorrer G, Wilson RE. *Fundamentals of Momentum, Heat, and Mass Transfer*. New Jersey: John Wiley & Sons; 2009.

58. Oh H, Lee Y, Lee G, Min K, Jung S. Experimental dissection of oxygen transport resistance in the components of a polymer electrolyte membrane fuel cell. *J Power Sources*. 2017;345:67-77.

59. Daian JF. *Equilibrium and Transfer in Porous Media 3: Applications, Isothermal Transport and Coupled Transfers*. New Jersey: John Wiley &Sons; 2014.

60. Kärger J, Ruthven D, Theodorou D. *Diffusion in Nanoporous Materials*. Weinheim: John Wiley & Sons; 2012.

61. Andisheh M, El Hannach M, Kjeang E, Bahrami M. An analytical relationship for calculating the effective diffusivity of microporous layers. *Int J Hydrogen Energy*. 2015;40(32):10242-10250.

62. Neale GH, Nader WK. Prediction of transport processes within porous media: diffusive flow processes within a homogeneous swarm of spherical particles. *AIChE J*. 1973;19(1):112-119.

63. Costa A. Permeability-porosity relationship: a reexamination of the Kozeny-carman equation based on a fractal pore-space geometry assumption. *Geophysical Research Letter*. 2006;33: L02318.

64. Espinoza M, Andersson M, Sundén B. Predicting transport parameters in PEFC gas diffusion layers considering micro-architectural variations using the lattice Boltzmann method. *Int J Energy Res*. 2017;41:565-578.

65. Sadeghifar H, Jilali N, Bahrami M. Effect of polytetrafluoroethylene (PTFE) and micro porous layer (MPL) on thermal conductivity of fuel cell gas diffusion layers: modeling and experiments. *J Power Sources*. 2014;248:632-641.

66. Pant LM, Mitra SK, Secanell M. Absolute permeability and Knudsen diffusivity measurements in PEMFC gas diffusion layers and micro porous layers. *J Power Sources*. 2012;206:153-160.

67. Kaviany M. *Principles of Heat Transfer in Porous Media*. Second ed. New York: Springer; 1991.